CRYSTAL GROWTH & DESIGN

pubs.acs.org/crystal

Article

Anisotropy of Barite during Crystal Growth and the Uptake of Radium

Stefan Rudin,* Piotr M. Kowalski, Martina Klinkenberg, Dirk Bosbach, and Felix Brandt

Cite This: *Cryst. Growth Des.* 2024, 24, 7774−7788

Read Online

ACCESS | Metrics & More | Article Recommendations | Supporting Information

ABSTRACT: The role of Ba^{2+} kink-site nucleation and step growth for the kinetics of anisotropic barite-(001) growth and Ra^{2+} kink-site nucleation for the activation energy of Ra uptake into the barite structure was investigated by using atomistic modeling approaches. The simulations show that Ba^{2+} kink-site nucleation at the barite-(001) water interface has higher activation energies at acute- and obtuse-low positions than at acute- and obtuse-high positions. The states at the low positions can be considered more relevant for barite crystal growth due to their higher stability. Kink-site nucleation at the obtuse step is preferred over that at the acute step due to the more open step geometry, which requires less dehydration. The simulations of the Ba^{2+}—step growth processes indicate a slow and uniform growth of the acute step and a faster anisotropic growth of the obtuse step. Ra^{2+} kink-site nucleation at barite-(001) exhibits increased activation energies due to lattice distortion, which is partially compensated by the easier dehydration of Ra^{2+} compared to Ba^{2+}. A small influence of Ra^{2+} on the kinetics of $(Ba,Ra)SO_4$ growth can be assumed because the rate-limiting kink-site nucleation process occurs preferentially through Ba^{2+} attachment compared to Ra^{2+} attachment. However, a preferential uptake of Ra^{2+} over Ba^{2+} during step growth, which requires a higher dehydration than kink-site nucleation, is therefore likely.

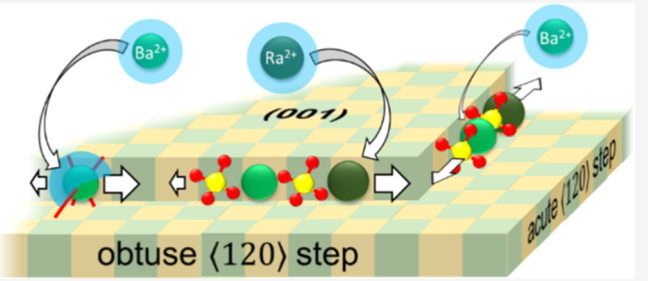

INTRODUCTION

The presence of ^{226}Ra in many mining-related processes, e.g. oil, gas, and coal extraction, and the formation of naturally occurring radioactive material (NORM) can lead to serious environmental problems.[1−4] In NORM, ^{226}Ra is often associated with barite ($BaSO_4$), due to similar ionic radii of Ba^{2+} and Ra^{2+}.[4] The fate of ^{226}Ra is also considered in safety assessments for the direct disposal of spent nuclear fuel. In some scenarios, the consequences of contact with the interstitial "in situ" pore water and spent nuclear fuel are investigated, suggesting that ^{226}Ra will make a significant contribution to the total dose after 10^4−10^5 years of waste disposal.[5] The formation of $(Ba,Ra)SO_4$ solid solutions is considered to be an important Ra-retention mechanism.[6−10] From the early study by Doerner and Hoskins[11] to more recent studies (e.g., refs 6−10,12−18), the formation of $(Ba,Ra)SO_4$ has been investigated experimentally. Weber et al.[18] suggested that ^{226}Ra is preferentially taken up during the recrystallization of barite, based on detailed transmission electron microscopy studies.

The crystal growth of pure barite has been studied experimentally using macroscopic and microscopic approaches (e.g., refs 19−25). Bosbach,[19] Pina et al.,[22] Pina et al.,[21] and Higgins et al.[20] studied barite crystal growth at the barite surface (001) at the molecular scale, which is considered the relevant surface for barite growth due to its high stability.[26−29] Crystal growth of barite is highly anisotropic, i.e., very different growth kinetics were observed in different crystallographic directions.[19−22,30] This leads to sector-shaped island growth along the ⟨120⟩ steps on the (001) surface, consisting of one curved fast-growing and two straight slow-growing steps.[19−22,30] The reason is that two types of steps ⟨120⟩ exist: obtuse steps with a step angle of 102° and acute steps with a step angle of 78° to the (001) surface[31] (Figure 1). de Antonio Gomez et al.[32] postulated on the basis of a similarly occurring step morphology in calcite that the obtuse barite (001) steps grow at higher rates than the acute steps. Kink-site nucleation, which is the attachment of the first ion to a (step-adatom) site, is considered to be the rate-limiting step for barite (001) growth.[21,33,34] From there, the step continues to grow anisotropically in both directions through the attachment of further ions at a step-adatom.[21] However, it is still debated whether Ba^{2+} or SO_4^{2-} kink-site nucleation is the rate-limiting step for barite growth.[21,30,33,35] Ba^{2+} and SO_4^{2-} kink-site nucleation can take place at four different sites due to a barite symmetry. A Ba^{2+} ion can attach at a high position at one site

Received: March 22, 2024
Revised: August 14, 2024
Accepted: August 27, 2024
Published: September 10, 2024

https://doi.org/10.1021/acs.cgd.4c00416
Cryst. Growth Des. 2024, 24, 7774−7788

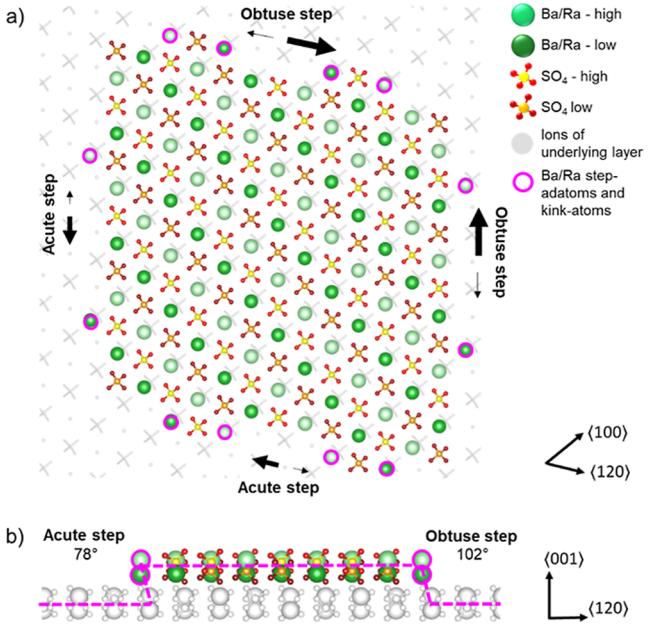

Figure 1. All possible sites for Ba^{2+} and Ra^{2+} kink-site nucleation and step growth at the ⟨120⟩ steps on barite (001). (a) Sites for Ba^{2+} and Ra^{2+} kink-site nucleation and step growth, view perpendicular (001). The sizes of the arrows indicate the postulated relative growth rate according to Pina et al.[21] and de Antonio Gomez et al.[32] (b) Sites for Ba^{2+} and Ra^{2+} kink-site nucleation, view parallel (001). The barite structures in the figures were visualized with the VESTA software.[36]

and a Ba^{2+} at a low position at the other site at each sulfate step-adatom, resulting in eight attachment sites (kink-atom positions) for further step growth in the ⟨120⟩ directions (Figure 1).

Simulation studies have attempted to link the mechanisms of crystal growth at the molecular scale to the macroscopic growth rates at the barite surface (001).[21,26,29,33,34] Pina et al.[21] used classical force-field-based molecular dynamics [classical molecular dynamics (CMD)] to simulate the final steps of Ba^{2+} and SO_4^{2-} kink-site nucleation and step growth at one [120] step on the barite (001) surface at different sites, considering water in form of experimental values, which were added to the energies obtained by the simulations. The different energies for kink-site nucleation and further ion attachment at different sites were considered to be the cause of anisotropic growth of the (001) face.[21] Stack[33] simulated the final step of Ba^{2+} and SO_4^{2-} kink-site nucleation at different sites using CMD with explicitly simulated water molecules and identified Ba^{2+} kink-site nucleation at a low position as the rate-limiting step.[33] Stack et al.[34] simulated for the first time a complete multistep Ba^{2+} kink-site nucleation process at the barite-water interface—starting with the fully hydrated Ba^{2+} ion up to the integration of Ba^{2+} into a ⟨120⟩ step on the (001) barite surface for one kink-site. Rudin et al.[29] applied an ab initio-based density-functional theory (DFT) and continuum solvation approach and were able to deliver activation energies and a similar reaction pathway for the Ba^{2+} kink-site nucleation process considered by Stack et al.[34]

Kink-site nucleation at other sites has not yet been fully simulated on a molecular scale. It is therefore still unknown, which kink-site nucleation processes are rate limiting. An interplay of kink-site nucleation and step growth processes on the molecular scale is assumed to be the reason for the anisotropic barite growth observed microscopically.[21,37,38] A description of all sites for barite step growth is also missing so far. The process of Ra^{2+} uptake into the barite structure has not yet been described at any site.

A direct comparison of the Ba^{2+} attachment and Ra^{2+} uptake processes at the molecular scale is therefore lacking. A different behavior of Ra^{2+} compared to Ba^{2+} due to the differences in the ion size and hydration energy can be assumed. Different relevance of the individual sites for Ra^{2+} uptake compared to Ba^{2+} attachment is also conceivable.

The aim of this study was to simulate the kinetics of the processes at the molecular level that lead to anisotropic barite growth and Ra^{2+} uptake into the barite structure. We were interested in the different behaviors of Ba^{2+} and Ra^{2+} during $(Ba,Ra)SO_4$ crystal growth. Therefore, this work focused on cation attachment during barite growth. Here, we used two different simulation methods: (1) classical force field-based (CMD)—simulations for quantitative sampling of different configurations of ions attached at different sites and (2) the DFT—continuum solvation approach tested and verified in Rudin et al.[29] to accurately simulate the complete Ba^{2+} and Ra^{2+} kink-site nucleation processes.

METHODOLOGY

Selection of Simulation Methods. The simulations performed in this study focus on processes at the obtuse and acute ⟨120⟩ steps at the barite (001) surface. A complete simulation of all Ba^{2+} and Ra^{2+} kink-site nucleation and step growth processes was not possible due to the large number of sites and resulting computational effort. Therefore, the final steps of Ba^{2+} kink-site nucleation and step growth were calculated first for all sites using computationally feasible CMD simulations with explicitly simulated water molecules. In addition, well-tested force fields already existed for the simulation of barite.[33,34,39,40] The computationally intensive DFT continuum solvation approach of Rudin et al.[29] was applied to simulate Ba^{2+} kink-site nucleation at all four sites. This choice was made because kink-site nucleation is postulated to be a rate-limiting process for barite crystal growth.[21,33,34] The barite surface is calculated with DFT, and the water was simulated implicitly using the soft-sphere continuum solvation (SSCS) method. The complete energy paths were calculated by using the nudged elastic band method (NEB). A comparison of the energies of the last steps for the Ba^{2+} kink-site nucleation allowed for a simultaneous comparison between CMD, and ab initio-based DFT—continuum solvation simulations and the comparison of implicitly and explicitly simulated water. For a direct comparison between Ba^{2+} and Ra^{2+}, the simulations of the complete kink-site nucleation were repeated at all sites for Ra^{2+} with the DFT continuum solvation approach.

Construction of the Simulation Cells of the Barite Surfaces. In order to verify the setup of the CMD simulations, a slab cell, as shown in Figure 2a was created. Here, a barite (001) surface slab including the ⟨120⟩ steps was constructed within a periodic cell containing 16 $BaSO_4$ formula units.

The remaining space was randomly filled with 397 explicit water molecules using the packmol software.[41] Different structures were created for the simulation of kink-site nucleation with CMD and selected configurations with DFT-SSCS, and the complete Ba^{2+} attachment processes with DFT-NEB-SSCS. The simulation cell of Rudin et al.[29] was used and modified. These were used to develop different structures

https://doi.org/10.1021/acs.cgd.4c00416
Cryst. Growth Des. 2024, 24, 7774−7788

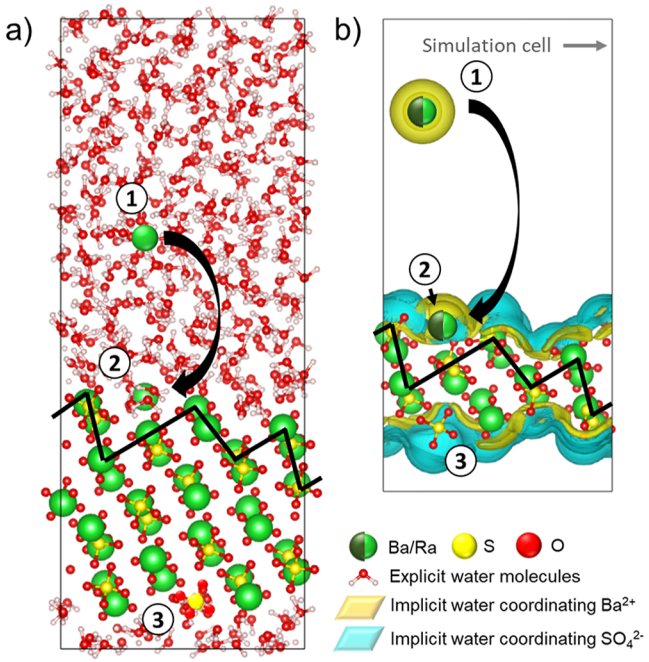

Figure 2. Simulation cells of the stepped barite (001)—water interface. (a) Simulation cell used for CMD simulations and (b) modified simulation cell according to Rudin et al.[29] (a) was filled up with explicit water molecules, in (b) implicit water was applied with the SSCS approach. (1) Ba^{2+} completely solved, (2) Ba^{2+} kink-site nucleation, and (3) SO_4^{2-} for charge compensation. The barite structures in the figures were visualized with the VESTA software.[36]

representing the initial, one intermediate, and the final state of each Ba^{2+}- and Ra^{2+}-ion attachment processes (Figure 2b). This cell was small enough to perform computationally expensive DFT-NEB-SSCS calculations, but it still contained all relevant attachment sites for Ba^{2+} and Ra^{2+} kink-site nucleation and further step growth. Periodic boundary conditions were applied in all three dimensions.[29] A vacuum layer, which was inserted between the slabs, was increased to form 15 Å in Rudin et al.[29] to about 20 Å to provide enough space for simulating the attachment process and to further minimize unwanted interactions between the barite slabs and/or the attaching ion. For the initial state, the attaching ion was fixed in a position in the middle between the periodically repeated slabs [Figure 2(1)] to simulate the completely dissolved ion. The configuration of the inner-sphere complex corresponding to Rudin et al.[29] was used as the intermediate state and relaxed. For the final state, the attached ion was placed at the corresponding ⟨120⟩ step on the slab [Figure 2(2)]. To maintain charge neutrality within the unit cell, an additional sulfate group was added to the bottom of each of the slabs in all structures (3). All structures used in this study are available in the data publication, as in ref 42.

Classical Molecular Dynamics Simulations. CMD simulations were carried out using the GULP simulation package.[43,44] Here, we used the MSXX force field of Jang et al.[39] and the modified F3C force field of Levitt et al.[45] used by Stack[33] for barite crystal growth simulations and implemented these in the GULP code. Test simulations with the setup from Stack and Rustad[40] resulted in lattice enthalpies for the bulk barite of −2489 kJ/mol. These are in good agreement with both the calculations of Stack and Rustad (−2480 kJ/mol)[40] and experimental data (−2478 kJ/mol).[39] In addition, hydration enthalpies of −40 kJ/mol were determined for the bulk water with the same setup as used in Stack and Rustad.[40] These are also in good agreement with both the simulations with Stack and Rustad (−42 kJ/mol),[40] and values determined from calorimetry measurements (−41.5 kJ/mol).[46]

The interactions between Ba^{2+} ions, S ions and $O_{sulfate}$ ions as well as their interactions with the H and O_{water} ions in the water molecules, which are caused by Van der Waals forces, were simulated using Buckingham potentials. The O_{water}−O_{water} and H−H interactions between different water molecules were simulated with a Lenard-Jones potential, while harmonic potentials were employed for S−$O_{sulfates}$ and O_{water}−H bonds. The orientation of the S−O and H−O bonds was described by three-body potentials and, in the case of SO_4, also by a four-body potential. The pair potentials of the interactions between two atoms in the simulations were calculated using a Lenard-Jones potential. The short-range forces were truncated at a distance of 10 Å.[33] The equilibration time was 200 ps. The subsequent CMD simulations were run for 1000 ps. The time step was 1 fs. The CMD simulations were performed using the canonical *NVT* ensemble.[47−49]

Set-Up of Hybrid DFT—Soft-Sphere Continuum Solvation Approach. While the barite crystal was simulated with ab initio DFT, the SSCS—method[50] was used to simulate hydration effects. The DFT simulations were performed using the Quantum-ESPRESSO package.[51,52] The same setup was applied here as in Rudin et al.[29] The PBE exchange correlation functional[53] was also used as the exchange correlation functional in all DFT calculations, which delivered the best agreement between the calculated and measured lattice parameters of the barite elementary cell in previous works.[29] Core electrons of the system were replaced by the ultrasoft pseudopotentials from Vanderbilt[54] and a plane energy threshold of 25 and 100 Ry was applied.

The structure of the bulk barite was verified in Rudin et al.[29] with data derived from X-ray diffraction (XRD).[55] In this study, the $RaSO_4$ bulk phase was also simulated and verified with the existing data from XRD measurements (Table 1).

Table 1. $RaSO_4$ DFT Volume Cell Relaxations and Comparison with Experimental Literature Data Derived from XRD Measurements of Matyskin, et al.[55]

cell parameter	this study (DFT)	literature data (XRD)[55]
a [Å]	9.15	9.129(8)
b [Å]	5.57	5.538(3)
c [Å]	7.35	7.313(5)
V [Å^3]	375.11	369.719

The determined values of the DFT simulations overestimate the $RaSO_4$ unit cell by only 0.02−0.04 Å in the corresponding directions and are, thus, in good agreement with the experimentally determined values. We note that it is expected that the PBE functional overestimates the lattice parameters[56] and the thermal expansion effects are not accounted for in the simulations.

Parameter Selection for DFT-SSCS—Simulations. DFT-SSCS simulations were performed using the Environ simulation package.[50−52,57,58] In the SSCS method, a radius is assigned to each explicitly simulated atom type defining the solvation sphere, representing the solvent from the explicitly simulated atoms.[50] The smooth transition from bulk water to a vacuum simulates the hydrated surfaces and hydrated shells of

https://doi.org/10.1021/acs.cgd.4c00416
Cryst. Growth Des. 2024, 24, 7774−7788

the solute ions. The solvent is described by the dielectric constant (ε = 78.4), controlled by the continuous switching function.[50] Hydration energies can be adjusted to experimental values by rescaling the radii of the species. On the one hand, the default values (e.g., the universal force field[59]) can be changed along with the scaling factor α, as done in Rudin et al.[29] On the other hand, the scaling of the solvation spheres can be specified manually for each atom type.[50] In this study, the radii for Ba^{2+}, Ra^{2+}, and SO_4^{2-} applied by Rudin et al.[29] were used and the values for Ra^{2+} were adjusted according to the literature values (refs 60 and 61).

Rudin et al.[29] showed that the relaxed structure of the barite-water interface follows the trends from experimental studies[62,63] and simulations.[62] The experimentally determined energy of the barite-(001)-water interface of 0.024 J/m^2 of Chibowski and Hołysz[64] could be well reproduced (0.022 J/m^2) applying an α-value of 1.27.[29]

In addition, the parameters for the electrostatic embedding effects for slab cells in the SSCS scheme are slightly different from those used by Rudin et al.[29] This approach was able to improve the values for the activation energies according to literature values,[19,20,65] while the sequence of minimum energy structures during kink-site nucleation and the hydration energies for the solvated ions were preserved according to Rudin, et al.[29]

Adjustment of Solvation Sphere for Simulation of the Hydrated Ra^{2+}-Ion. Experimentally determined hydration enthalpies in the literature differ significantly from each other. While Marcus[66] postulated that Ba^{2+} and Ra^{2+} have the same hydration enthalpies of 1250 kJ/mol, Smith[61] claimed that Ra^{2+} has a lower hydration enthalpy of 1266 kJ/mol than Ba^{2+} of 1305 kJ/mol. A lower hydration enthalpy of Ra^{2+} compared to Ba^{2+} is likely because of the higher water coordination number in the first hydration shell of Ra^{2+} at the same charge due to the larger size of Ra^{2+}.[60] This could lead to easier dehydration. Housecroft and Brooke Jenkins[67] were able to show that there is a linear relationship between the ion volume of ($V^{-1/3}$) and the hydration enthalpy for alkali metal ions. Figure 3 shows the ion volume versus the hydration enthalpy for the alkaline earth metal ions, with values from the literature indicating a linear relationship between ΔH and $V^{-1/3}$. The values for the hydration enthalpies from Smith[61]

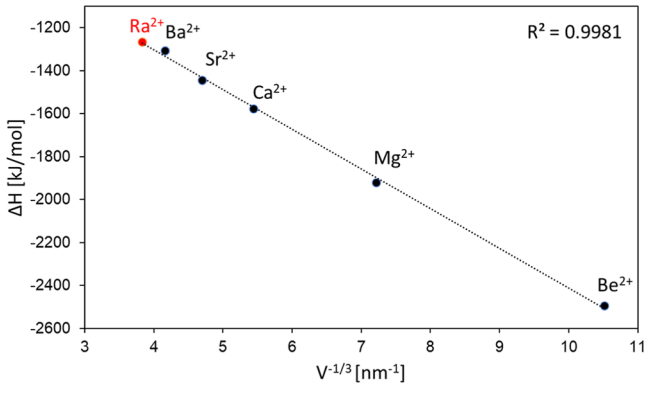

Figure 3. Hydration enthalpy of formation versus ion volume ($V^{-1/3}$) for alkaline earth metals, adapted from studies of Housecroft and Brooke Jenkins.[67] The hydration energies are from Smith,[61] the ion radii from Shannon.[60] The trendline does not include the value for Ra^{2+} to determine if the value for $\Delta H_{Ra^{2+}}$ follows the trend.

follow this trend. The hydration enthalpies ΔH for Ra^{2+} can therefore be assumed to be realistic.

Simulations of the complete Ba^{2+} and Ra^{2+} kink-site nucleation pathways were achieved using the hybrid DFT-NEB-SSCS approach of Rudin et al.[29] An α-value of 1.27 was used for the implicit water simulation as this best represents the surface free energy of the barite (001)-water interface. However, the hydration energy of the Ba^{2+} ion is underestimated (Table 2 and Rudin et al.[29]). An α-value of 1.27 with

Table 2. Adaptation of Ra^{2+} Hydration Energies and the Radius of the Solvation Sphere to the Values of Ba^{2+} with an α-Value of 1.27, Considering the Literature Values

	solvation sphere radius	hydration shell radii	hydration enthalpies ΔH	
	[Å]		[kJ/mol]	
	this study	literature values	this study	literature values
Ba^{2+}	4.70	2.6−2.86[68−76]	916.68	1305[61]
Ra^{2+}	4.83	2.85−2.93[74,77]	877.34	1266[61]
ratio	1.03	0.997−1.127	1.04	1.03
difference			39.34	39

the setup used by Rudin et al.[29] corresponds to a manually adjusted solvation sphere radius of 4.70 Å (Table 2). The Ra^{2+} value was adjusted so that the ratio and the difference in hydration enthalpy in the SSCS simulations between Ra^{2+} and Ba^{2+} (α = 1.27) match the literature values. The ratio of the adjusted solvation sphere radii also corresponds to the ratio of the first hydration shell of fully dissolved Ba^{2+} and Ra^{2+} in water according to the literature (Table 2).

Climbing Nudged Elastic Band Method. The energy paths describing the ion attachment processes were simulated using the NEB method as implemented in the Quantum-ESPRESSO package.[51,52,78−82] The climbing image method (Cl-NEB)[80] was used to ensure that the highest value of each energy pathway, and thus the crucial transition states describing the activation energies for each ion attachment process were accurately described. Due to their complexity, the calculations were each split into two paths. The start- and inner sphere complexes or the inner sphere complex and the end-structure were used as the start- and end-structure, respectively. Moreover, because two transition states were found to be particularly relevant in each case in Rudin et al.,[29] this approach assured an accurate simulation of both transition states with Cl-NEB. The two partial pathways were calculated with 15 and 20 images, respectively.

Estimation of the Entropy Contribution to the Computed Energies. For estimating the contributions of the entropy on the activation energies for the Ba^{2+} and Ra^{2+} attachment processes, we applied the two-phase thermodynamic (2PT) method.[84−86] This method has been recently used by Cheong et al.[83] to estimate the entropy of aqueous species in the bulk water and at aqueous interfaces with the computed values well consistent with the measurements.[83] The 2PT method calculates the entropy of solvated species from the density of states (DOS) derived from the Fourier transform of the velocity autocorrelation function.[84−86] The analysis of the obtained frequency spectra allows for decomposition of the DOS function into the vibrational, translational, and rotational modes, and computation of the related entropic contributions.[85]

https://doi.org/10.1021/acs.cgd.4c00416
Cryst. Growth Des. 2024, 24, 7774−7788

For the 2PT calculations, we used the same cell as for the main CMD simulations (Figure 2a) and performed the analysis on the trajectories derived by the CMD simulations. These were equilibrated for 20 ps with a production run of 20 ps and a sampling time step of 2 fs, as applied in previous aforementioned studies.

RESULTS AND DISCUSSION

Ba^{2+} and Ra^{2+} Kink-Site Nucleation: Comparison of Initial Steps, Inner Sphere Complexes, and Final Steps. *Ba^{2+} Kink-Site Nucleation: Initial Steps, Inner Sphere Complexes, and Final Steps.* Figure 4a summarizes the

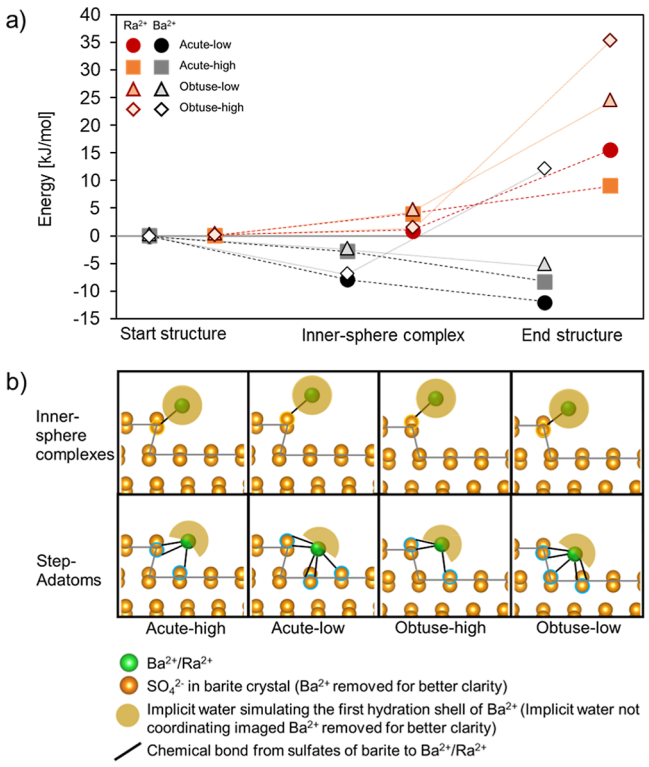

Figure 4. (a) Energies of the main minimum energy configurations occurring during the binding of Ba^{2+} and Ra^{2+} at different positions on the ⟨120⟩ steps on the barite surface (001). The values are normalized to the lowest value of the start-structures for both Ba^{2+} and Ra^{2+}, (b) Ba^{2+} and Ra^{2+} inner sphere complexes (according to Rudin, et al.[29]), and kink-sites at different positions on the ⟨120⟩ steps.

energies of the ions fully dissolved in water (start structures), the inner sphere complexes, and the configurations of complete uptake at the corresponding step-adatom position (end structures) for kink-site nucleation of Ba^{2+} and Ra^{2+} at all four positions, which are shown in Figure 1. Almost identical energies of the start structures were calculated. An influence of the different step morphologies of the barite surface on Ba^{2+} with a distance of ∼ 10 Å can therefore be excluded. A correct description of the Ba^{2+} ions completely dissolved in water in bulk water can therefore be assumed. The energies of the inner sphere complexes for acute-high and obtuse-low as well as acute-low and obtuse-high are also quite similar. The first two are each associated with a SO_4^{2-} at the high position, whereas the other two are each associated with a sulfate at the low position (Figure 4b). As already shown in Rudin et al.,[29] the energies of the inner sphere complexes are thus mainly controlled by the sulfate position within the step and not by the barite surface topography.

Step-adatoms at the high and low positions of the acute step are each more dehydrated than the adatoms at the corresponding sites of the obtuse step because they are closer to the barite surface (Figure 4b). Within the steps, step adatoms at the high sites are connected via three bonds to two sulfates, but step atoms in the low positions via five bonds to three sulfates. This is consistent with the CMD-simulations of the step-adatoms at the acute step by Stack,[33] using the same force-fields for their simulations as we have applied here. A higher number of bonds of the Ba^{2+} ion to the barite structure is associated with a higher degree of dehydration. In the case of ions at the barite-water interface, bonds to other ions that are missing compared to ions in the bulk structure are compensated by the coordination of water molecules.[33,34]

The different degree of hydration of adatoms at the acute and the obtuse step can be explained by a steric hindrance, as already described by Stack,[33] who compared different sites at the acute step. Due to the different step morphologies, the space for the coordinating water at the step-adatom of the acute step is more limited than at the obtuse step.[32] Because the Ba^{2+} kink-sites are closer to the barite surface in the low position, the steric hindrance is more pronounced there. The higher energies of the high sites compared to the low sites are consistent with the Kossel-Stranski model.[87,88] According to this model, more bulk-like positions, which contain a higher number of direct neighboring atoms/ions, are energetically more favorable, promoting crystal growth.[87,88] The step geometry has a stronger impact on the energies of the configurations than the number of neighboring ions. However, different step geometries, caused by the orthorhombic symmetry of barite, are not described by the Kossel-Stranski model, only the simpler cubic system.[87,88] The thermodynamically favored sites at the acute positions are in contradiction to the work of de Antonio Gomez et al.,[32] who expected the obtuse step to be the fast-growing one, as analogously observed in calcite growth.[89−91] Therefore, kinetic effects are likely to be responsible for the faster growth of the obtuse step.

Ra^{2+} Kink-Site Nucleation: Initial Steps, Inner Sphere Complexes, and Final Steps. The start structures, inner sphere complexes, and end structures for Ra^{2+} kink-site nucleation simulated with DFT-SSCS resulted in similar morphologies as for Ba^{2+} kink-site nucleation (Figure 4b). Similar systematic energy differences can be seen for the start structures and inner sphere complexes, as previously discussed for the corresponding Ba^{2+} structures (Figure 4a). However, in contrast to the corresponding Ba^{2+} configurations, the end structures and Ra^{2+} inner sphere complexes all exhibit energies higher than those of the corresponding start structures. This is due to a lattice distortion caused by the slightly larger diameter of the Ra^{2+} ion compared to that of the Ba^{2+} ion.

A higher number of direct neighboring ions results in a higher lattice distortion and thus higher energy. In contrast to the Ba^{2+} step-adatoms, the simulations indicate lower energies at the acute-high site than at the acute-low site, for the Ra^{2+} step-adatom, due to higher lattice distortion, which is caused by a higher number of direct neighbors. However, the Ra^{2+} step-adatoms at the acute sites both have lower energies than the step atoms at the obtuse sites. The step morphologies thus also exert a stronger influence on the energies in the case of Ra^{2+} than the number of direct neighbors. The Ra^{2+} step-adatom at the obtuse-high site could be simulated only by

https://doi.org/10.1021/acs.cgd.4c00416
Cryst. Growth Des. 2024, 24, 7774−7788

fixing the Ra^{2+} position. The release of the positions leads to the detachment of Ra^{2+} and the formation of an inner sphere complex. This indicates that this Ra^{2+} kink-site has no energy minimum and is therefore unstable. The simulations of the Ra^{2+} step-adatoms at the other sites state an energy minimum and are thus (meta)stable.

Comparison of Step-Adatom Energies with Classical MD versus DFT-SSCS. The energies of the last steps of Ba^{2+} kink-site nucleation simulated with CMD according to Figure 1 are listed in Table 3. The comparison of the simulations for the fully attached adatoms revealed systematic energy differences between them. The Ba^{2+} step-adatom at the acute-low position had the highest energy calculated with DFT-SSCS, but the lowest values in the CMD-simulations. The higher energies could be caused by a sterical hindrance.[33] This prevents the complete compensation of the Ba^{2+} bonds in the step-adatom position by the coordination of water molecules, which are missing in the bulk structure compared with the fully incorporated ion. The step-adatom at the obtuse-high site detached during the CMD-simulation period and forms an inner sphere complex with lower energy.

Table 3. Energy Differences between Ba^{2+} Step-Adatoms and the Start-Structures (See Figure 2) at All Sites of the ⟨120⟩ Steps of the Barite (001)-Water Interface (See Figure 1) as Computed by CMD- and DFT-SSCS Simulations[b]

	Ba^{2+} kink-site nucleation ΔE [kJ/mol]	
site	CMD	DFT-SSCS
acute-low	−2.56	−12.10
acute-high	−32.55	−8.23
obtuse-low	−19.06	−5.01
obtuse-high	−22.81[a]	12.23

[a]Detachment during simulations. [b]A negative sign indicates an exothermic reaction for kink-site nucleation.

The total energies of the Ba^{2+} step-adatom configuration determined from the CMD-simulations thus reflect a combined energy from both configurations. The transition of the inner sphere complex to complete kink-site nucleation is therefore an endothermic reaction, which is also postulated by the DFT-SSCS simulations. Furthermore, the energies of the Ba^{2+} step-adatom at the acute-high are slightly lower than the energies of the Ba^{2+} step-adatom at the obtuse-low site in both the DFT-SSCS and the CMD simulations. The energies are reasonable in comparison to Stack et al.,[34] who computed the energy differences between start-structure and end-structure in that way. Furthermore, both sites require similar dehydration, obtuse-low due to the closer proximity to the step and acute-high due to the geometry of the step, which additionally lowers the energy of the step-adatom at the acute-high site.

Kinetics of Anisotropic Barite (001) Crystal Growth. *Kinetics of Ba^{2+} Attachment from the Fully Detached Hydrated Ion to the Kink-Site Nucleation.* Figure 5 shows the energy paths for the complete Ba^{2+} kink-site nucleation processes from fully dissolved to fully attached ions at all possible sites at the ⟨120⟩ step of the barite-water interface (001), as shown in Figure 1. The individual steps of kink-site nucleation at the acute high- and obtuse-low steps are shown in Figure 5c.

Four pathways were identified whose trajectories increasingly differ as Ba^{2+} attachment progresses. All Ba^{2+} attachment pathways contain two major energy barriers and different activation energies (Table 4).

The second energy barrier is the highest in all cases except for kink-site nucleation at the acute-high site and thus is also the rate-limiting step. Due to the lower energies of the inner sphere complexes compared to the start structures, the total activation energies mainly depended on the transition from the inner sphere complex to the complete attachment. The chemical bond formation was accompanied by a simultaneous stepwise dehydration, which are largely compensating each other.[29,33,34] These processes contribute most to the energy pathways, as observed in previous studies of simulations of Ba^{2+} kink-site nucleation at the acute-low step.[29,34] The dehydration of part of the barite-water interface, to which the ion is bound, also plays a role and increases the activation energy. In addition, the attaching ion influences the barite structure during kink-site nucleation, resulting in the lattice distortion (Figure 5c).

Ions that form only a few bonds to other ions of the barite structure due to their exposed position are more affected by the distortion than ions that have more bonds to the residual of the barite surface. The SO_4^{2-} ion in the high position of the obtuse step only form three bonds to Ba^{2+} ions in the barite structure on the relaxed stepped barite (001) water interface with ⟨120⟩ steps. It is therefore the anion that is most weakly bound to the remaining barite structure at the barite-water interface, which leads to a large displacement and rotation of this ion during kink-site nucleation at the obtuse-low position simulated in this study. As a result, bonds are broken and new ones are formed, which leads to an increase in the activation energy for kink-site nucleation processes at the obtuse-low site.

The individual steps are similar at all four sites up to the formation of the inner sphere complex. The steps during kink-site nucleation at the high and low sites are the same in both cases (see Figure A1[42]). The main difference between the formation of kink sites on the acute and obtuse steps at the respective high and low sites is the slightly lower dehydration at the obtuse steps due to the different step morphologies. This difference is more pronounced between the low sites as these are closer to the ⟨120⟩ step than the step adatoms on the high sites (see Figure 4b).

The first steps show slight energy minima, which include the formation of an outersphere complex [Figure 5c(2)]. The first large energy barrier is caused by the formation of a chemical bond to a sulfate in a high part of the step together with partial dehydration (3). In the following step, a bidentate complex is formed in all cases of kink-site nucleation at a low site by the formation of a second chemical bond to a second oxygen on the same sulfate (4). In the next step, at all sites and a high position, two bonds to two different sulfates are formed. At the obtuse-low site, an additional chemical bond to another sulfate is formed. It results in a tridentate complex in all three cases (5). At the acute-low site, two bonds to one further sulfate are formed [Figure A1(7,8)]. These steps are accompanied by a rotation of the sulfate already chemically bonded to the Ba^{2+} ion and further shifts of the ions within the barite structure. During kink-site nucleation at the high sites, besides small displacements of the attaching Ba^{2+} ion and ions in the barite structure, this is the last step (5,6). In contrast, kink-site nucleation at the obtuse-low position requires the simultaneous formation of two further chemical bonds to the barite surface (7−9), during kink-site nucleation at the acute low-site, one more bond is formed to one further sulfate [Figure

https://doi.org/10.1021/acs.cgd.4c00416
Cryst. Growth Des. 2024, 24, 7774−7788

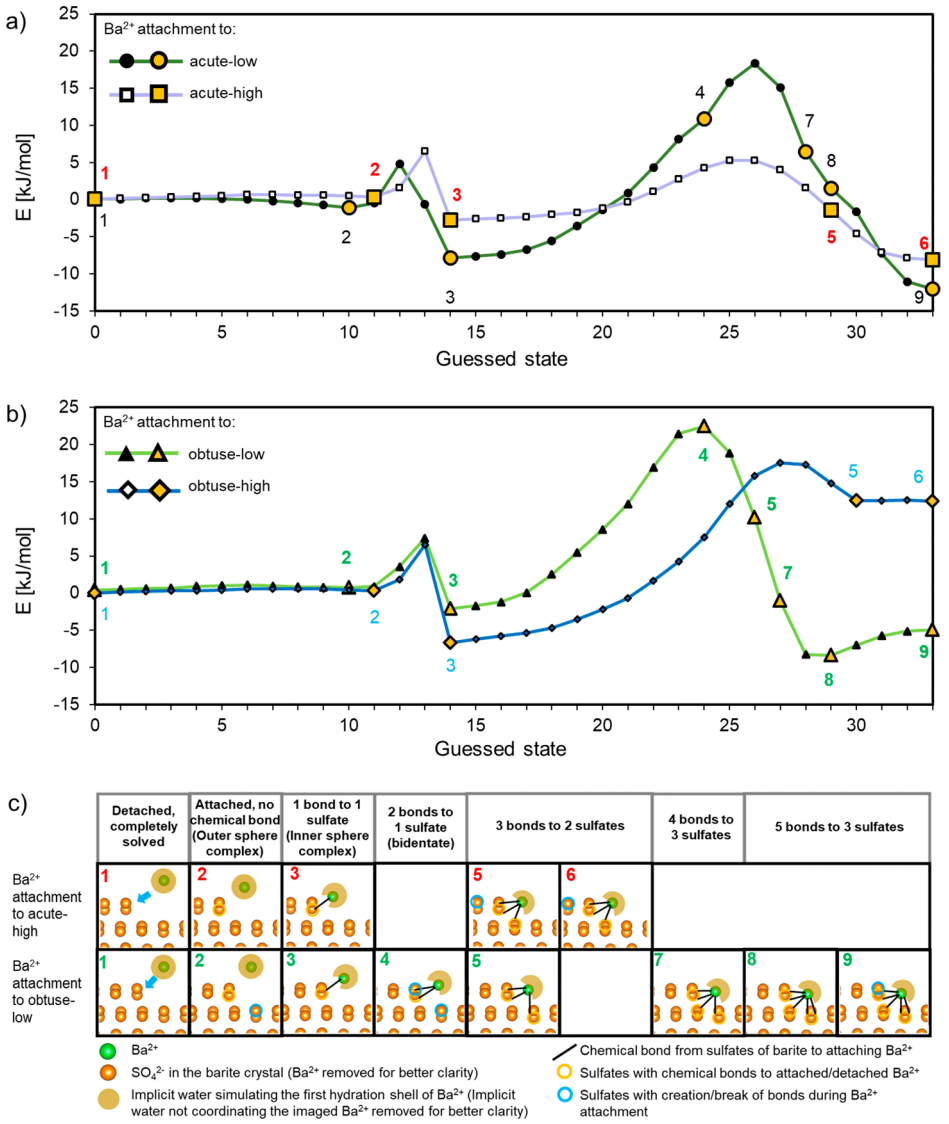

Figure 5. Comparison of the attachment pathways of Ba^{2+} kink-site nucleation (a) at the acute step and (b) at the obtuse step. The energy of the fully dissolved ion (guessed state 0) is set to 0 in all cases; (c) comparison of the guessed states of the acute-high and obtuse-low steps highlighted in (a,b).

Table 4. Activation Energies for the Nucleation of Ba^{2+} and Ra^{2+} at all Sites on the ⟨120⟩ Steps of the (001) Surface

	[kJ/mol]	acute-low	acute-high	obtuse-low	obtuse-high
Ba^{2+}	attachment	26.15	8.04	24.59	24.23
	detachment	30.33	14.63	27.41	13.18
Ra^{2+}	attachment	30.18	13.92	37.60	35.26
	detachment	14.66	4.86	13.36	4.44

A1(9)]. The presence of two end structures at the obtuse-low [Figure 5b(8,9)] and obtuse-high [Figure 5b(5,6)] sites is due to the easy rotation of a sulfate within the barite structure. These configurations can easily merge due to the low activation energies in between.

The simultaneous formation of two bonds during the kink-site nucleation process can be interpreted as the close temporal succession of bonds.

Correlation of Bond Length and Energy Paths. The bond lengths of the step atoms are given in Table 5. The Ba^{2+} step-adatoms at all sites have the shortest bond to the single sulfate, while it has an intermediate length for the step atom at the obtuse-high site. This single bond is formed last or broken first during detachment in all kink-site nucleation simulations in this study, except for kink-site nucleation at the obtuse-low position. In contrast, in Stack et al.,[34] two bonds to two different sulfates are formed first during the bidentate complex formation or are broken in the same order during detachment at the acute-low site.

The attachment pathway for kink-site nucleation at the obtuse-low step is plausible, as the longest bond is formed last, and longer bonds can be considered less stable than shorter bonds. During the kink-site nucleation at the acute-low step, the SO_4^{2-} ion, to which the last bond is formed, has the least number of bonds to the residual barite surface [see Figure A1, (8) circled in blue]. The Ba^{2+} thus exerts the largest displacement by attracting the sulfate ion to the attached step-adatom, which shortens the chemical bond in the final steps of kink-site nucleation. Upon detachment, a single bond between a Ba^{2+} adatom and a SO_4^{2-} could be more easily affected by a water molecule, as it is more accessible than two bonds.[33,34,62] At the acute-high site, the formation and

https://doi.org/10.1021/acs.cgd.4c00416
Cryst. Growth Des. 2024, 24, 7774−7788

Table 5. Bond Length of Fully Attached Ba^{2+} and Ra^{2+} during Kink-Site Nucleation as Imaged in Figure 3[a]

	bond length [Å]	acute-low	acute-high	obtuse-low	obtuse-high
Ba^{2+}	sulfate-high	2.85	2.72	2.71	2.63
		2.89	2.82	2.74	2.81
	sulfate-low1	2.72	2.65	2.76	2.73
		2.77		2.97	
	sulfate-low2	2.67		2.65	
Ra^{2+}	sulfate-high	3.12	2.92	2.89	
		3.02	3.10	2.96	no stable configuration
	sulfate-low1	2.93	2.89	2.96	
		2.97		3.09	
	sulfate-low2	2.91		2.88	

[a]Ba^{2+} ions have bonds to one sulfate on the high position of the ⟨120⟩ step: sulfate-high, and one or two sulfates in the low part of the step: sulfate-low1 and sulfate-low2.

dissolution of the adatom and the inner sphere complex require similar activation energies; although the former involves the breaking/formation of more bonds as well as higher (de)hydration. Aggravating conditions for the dissolution of the inner sphere complex, as postulated in Stack et al.,[34] are therefore likely.

Relevance of Different Kink-Site Positions for the Crystal Growth of Barite (001). Step-adatoms at the acute site and especially at the low step are thermodynamically more favorable than sites that are located further away from the step due to the steps and site morphologies. However, the reaction pathway demonstrates a higher complexity and therefore requires a higher activation energy. Step-adatoms at acute-high sites are kinetically preferred as the activation energy for kink-site nucleation is lowest there. However, barite crystal growth at the molecular site is characterized by back-and-forth reactions.[34,38,92,93] The activation energies for the detachment of kink-sites do not indicate the dissolution of barite crystals, as the detachment of a positive kink-site is not postulated as a rate-limiting step for barite dissolution.[25,30] However, low activation energies for the back reaction indicate an easy detachment of step-adatoms at high sites compared to those at low sites. The detachment of step-adatoms at the acute and obtuse sites requires very little hydration, and only two bonds need to be broken to form the corresponding inner sphere complex. Due to the more open geometry, the effect of water on the chemical bonds is likely enhanced.

Barite step growth requires the addition of further ions.[21,30,33,34] The kink-site nucleation of Ba^{2+} shows that SO_4^{2-} is also influenced within the barite structure in the form of large lattice shifts and bond breaks, as shown in this study and Rudin et al.[29] A large influence on the step-adatom by the approach of negatively charged SO_4^{2-} ions during further step growth is therefore plausible. An at least partial detachment of step-adatoms at high sites only connected to the barite surface by a low number of chemical bonds is therefore probable. The stability of this configuration up to and during further ion attachment during step growth is therefore questionable. This assumption is also supported by the CMD simulations in this study, in which the detachment of the Ba^{2+} kink-site at the uppermost position occurred during a simulation time of 1000 ps.

Kink-site nucleation but also the detachment of step-adatoms at the acute-low and obtuse-low sites require high activation energies. This leads to high stability. A further attachment of additional SO_4^{2-} ions is therefore more likely than a Ba^{2+} step-adatom at a high-site. The importance of the low position kink-sites for the crystal growth of the barite-(001)-water interface can therefore be estimated to be higher. Considering only the step-adatoms at the low sites and Ba^{2+} kink-site nucleation as rate-limiting steps for both acute and obtuse step growth, kink-site nucleation at the obtuse step is preferred due to the lower required dehydration. This could lead to faster growth of the obtuse step, which corresponds to the growth of calcite crystals,[89−91] as also postulated in the literature for barite.[32]

Barite ⟨120⟩ Step Growth and Relevance of Different Sites for the Anisotropic Growth of Barite (001). The simulations indicate that kink-sites for step growth are energetically more favorable than those for kink-site nucleation (Tables 3 and 6). According to the Kossel-Stranski model, sites with more neighbors are expected to have lower energies.[87,88] The step adatoms for kink-site nucleation contain two neighbors, and the sites for further step growth are surrounded by three.

Table 6. Relative Energies of Ba^{2+} Sites (Kink-Atoms) for Further Step Growth at All Sites of the ⟨120⟩ Steps of the Barite (001)-Water Interface Computed by CMD-Simulations[a]

Ba^{2+} step growth		
SO_4-kink-site	site	ΔE [kJ/mol]
acute-low	low	−42.63
	high	−70.69
acute-high	low	−26.10
	high	−53.68
obtuse-low	low	−58.12
	high	−5.46
obtuse-high	low	−49.91
	high	−31.70

[a]The numbers are the difference from the value of the respective start-structures computed with CMD (see Figure 2a). The position of the SO_4^{2-} to which the Ba^{2+} is attached is given first, followed by the position of the Ba^{2+} itself (see Figure 1).

Based on these results of this study, a faster kink-site nucleation at the obtuse step appears likely. However, the sites for step growth by the addition of a Ba^{2+} ion have, on average, lower energies at the acute step than at the obtuse step (Table 6).

The positions for step growth at the acute step, which have the lowest energies, are all high positions (Figure 1). Thus, a low degree of dehydration is likely to be necessary during the

https://doi.org/10.1021/acs.cgd.4c00416
Cryst. Growth Des. 2024, 24, 7774−7788

attachment. In accordance with the results for kink-site nucleation from this study, low activation energies are therefore to be expected. Due to the high energies during kink-site nucleation at the acute step and low energies during step growth in the ⟨120⟩ direction, slow formation of the steps and rapid growth in the ⟨120⟩ direction can be expected. The result would be a slow growth of the acute step perpendicular to the ⟨120⟩ direction with a straight step morphology.

Considering the obtuse-step, a rapid kink-site nucleation can be expected based on this study. The different energies for the different sites for Ba^{2+} attachment to the kink-atom positions suggest a preferred growth direction of the obtuse step along the ⟨120⟩ direction. The formation of a curved step is therefore probable. Due to the preferential rate-limiting kink-site nucleation at the obtuse-step, a rapid growth of this step perpendicular to the ⟨120⟩ direction can be assumed. To summarize, this agrees well with the observations of anisotropic sector-shaped island growth in barite (001), which is often observed in microscopic studies (e.g., ref 19−22) (Figure 6).

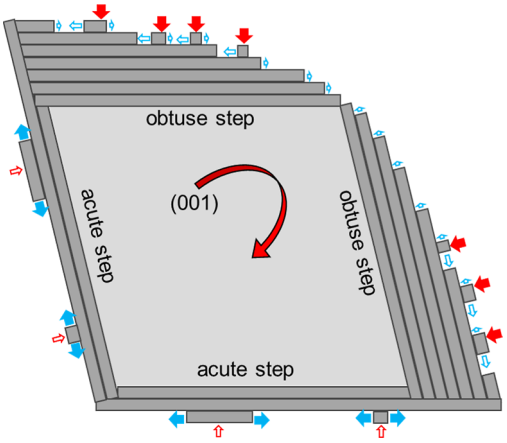

Figure 6. Illustration of the presumed growth of the barite (001) growth islands based on the DFT-NEB-SSCS and CMD simulations of the Ba^{2+} ion attachment process at step-adatom positions and kink-sites in this study. The rate-limiting processes of ion attachment at step-adatom positions (=kink-site nucleation) are shown with red arrows, the further step growth by ion attachment at kink-site layers is shown with blue arrows. The size of the arrows indicates the probability of the corresponding events.

Kinetics of Ra^{2+} Uptake into $(Ba,Ra)SO_4$−−H_2O System. *Ra^{2+} Kink-Site Nucleation Processes and Comparison to Ba^{2+} Kink-Site Nucleation.* The energy paths of the complete Ra^{2+} kink-site nucleation processes computed with the DFT-NEB-SSCS approach are shown in Figures 7 and A2[42] and are compared with the Ba^{2+} kink-site nucleation at the same sites (see Figure 5).

During Ra^{2+} kink-site nucleation, both the bonds and the order in which they are formed are almost identical compared to the corresponding Ba^{2+} kink-site nucleation processes. However, the individual intermediate structures contain different energies (Figure 7c). These differ increasingly from the corresponding energies of Ba^{2+} kink-site nucleation as the distance of the ion from the barite surface decreases (5−8). Larger differences emerge due to the step morphology, which requires larger dehydration during kink-site nucleation at the acute steps than at the obtuse steps.

Similar to Ba^{2+} kink-site nucleation, two large energy barriers exist. The latter is the highest in all cases except for kink-site nucleation at the acute-high site. However, the activation energies at all sites are higher than for Ba^{2+} kink-site nucleation at the corresponding site but reveal the same systematics (Tables 3 and 6). In contrast to Ba^{2+} kink-site nucleation, the higher energies of the inner sphere complexes compared to those of the respective start structures make the total activation energy dependent on the entire attachment pathway.

Ra^{2+} kink-site nucleation presents an equal systematics as Ba^{2+} kink-site nucleation at the corresponding sites; however, the activation energies are higher for Ra^{2+} kink-site nucleation in all cases (Table 4). Both the formation of Ra^{2+} inner sphere complexes (see Figure 7) and complete kink-site nucleation processes are endothermic reactions at all four sites. The activation energies for the detachment of the Ra^{2+} step-adatoms are therefore lower than those for the Ra^{2+} kink-site nucleation and also lower than the energies required for the detachment of the corresponding Ba^{2+} step adatoms. The main difference between Ra^{2+} and Ba^{2+} kink-site nucleation is the lower activation energy at the acute-low step compared to the obtuse-steps in the case of Ra^{2+} attachment.

Furthermore, the energy pathway for Ra^{2+} kink-site nucleation at the obtuse-high position does not show an energy minimum. This is consistent with the results of the simulations of the corresponding Ra^{2+} step-adatoms, which could not be stabilized. Consequently, Ba^{2+} kink-site nucleation and the detachment of the Ra^{2+} step-adatom is favored.

Comparison of Ba^{2+} and Ra^{2+} Pathways. The Ra^{2+} step ad-atoms contain longer bonds to the residual barite surface than the corresponding Ba^{2+} step ad-atoms (Table 5). However, the same systematics of relative bond lengths can be recognized. Attachment pathways for Ba^{2+} and Ra^{2+} kink-site nucleation processes at each site in which the same intermediate structures were obtained in the same order as in this study are thus plausible. The determined bond lengths of the Ra^{2+} step atom at the obtuse high site to the barite surface are not meaningful because the position of the Ra^{2+} ion was fixed in the a and *c* directions during the simulation (see Figure 2). No influence of the lattice distortion on the systematics of ion displacement can be noticed. Ions, which are bound to the barite structure by fewer bonds, are displaced more strongly by the Ra^{2+} kink-site.

Competition between Ba^{2+} Attachment and Ra^{2+} Uptake in Barite (001) and Influence on Barite Crystal Growth. Different reaction pathways between Ba^{2+} and Ra^{2+} kink-site nucleation is mainly caused due to different ion sizes and different hydration shells (see Figures 5 and 7). The slightly larger diameter of the Ra^{2+} ion (162 pm)[60] compared to Ba^{2+} (149 pm)[60] leads to lattice distortions at all sites during the Ra^{2+} uptake. Lower activation energies during the formation of the Ra^{2+} inner sphere complexes could indicate a possible easier partial dehydration. Lattice distortions are particularly relevant in the final steps of kink-site nucleation, where the influence between the stepped barite structure and the ion to be attached is the largest. The additional energies caused by ionic displacements and rotations of SO_4^{2-} in the barite structure are responsible for the increased activation energies compared to the Ba^{2+} kink-site nucleation at all sites.

Ra^{2+} step-adatoms that are closer to the barite structure require a higher lattice distortion than Ra^{2+} step-adatoms that are farther away due to the different step and site morphology.

https://doi.org/10.1021/acs.cgd.4c00416
Cryst. Growth Des. 2024, 24, 7774−7788

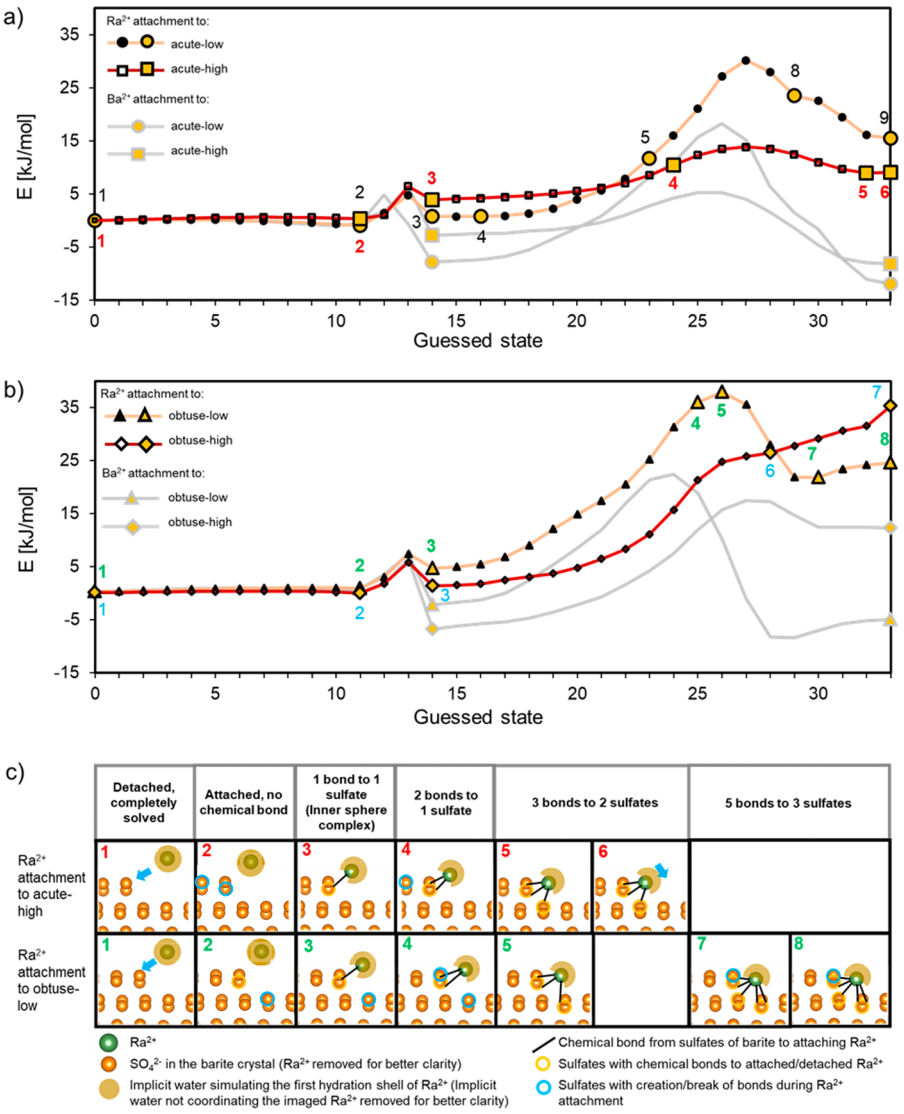

Figure 7. (a) Comparison of the attachment pathway of Ba^{2+} and Ra^{2+} kink-site nucleation at the acute step. (b) Comparison of the attachment pathway of Ba^{2+} and Ra^{2+} kink-site nucleation at the obtuse step. The energy of the fully dissolved ion (guessed state 0) is set to 0 in both cases. (c) Comparison of the guessed states highlighted in (a,b).

The highest lattice distortion requires kink-site nucleation at the acute-low position. Therefore, the largest energy differences between Ra^{2+} and Ba^{2+} kink-site nucleation should be expected at this site. However, the DFT-NEB-SSCS simulations show that Ra^{2+} kink-site nucleation processes at sites closer to the barite structure have activation energies more similar to those of the corresponding Ba^{2+} kink-site nucleation. The activation energies of Ra^{2+} kink-site nucleation at sites further away from the ⟨120⟩ steps of the barite exhibit larger differences from Ba^{2+} kink-site nucleation at the corresponding sites. Considering only the activation energies between the inner sphere complex and the complete kink-site nucleation at the acute-low position, they are almost identical. Because kink-site nucleation at this position requires the largest dehydration of the attaching ion, it is likely that Ra^{2+} dehydrates more readily than Ba^{2+} during attachment. Consequently, a higher necessary dehydration could compensate for the energy of lattice distortion during the Ra^{2+} uptake.

Ra^{2+} uptake at sites that are only weakly connected and far away from the barite surface can be excluded for the relevance of Ra uptake. The reason for this is that the activation energies are significantly higher than those for the corresponding Ba^{2+} kink-site nucleation. Due to the low dehydration, the higher energies caused by the lattice distortion cannot be compensated. The low dehydration and the formation of few bonds favor the exothermic back reaction and thus the dissolution. This is also the reason the Ra^{2+} kink-site at the obtuse-high site is not stable.

According to the trends found in our study regarding kink-site nucleation, for the step growth sites, a lower activation energy can be assumed for Ra^{2+} uptake than for Ba^{2+} attachment. The reason is the higher number of nearest neighbors.[87,88] The lattice distortion in the Ra^{2+} uptake can therefore also be considered more pronounced, but the Ra^{2+} uptake could be advantageous, as higher dehydration is also required.

In addition, the model of Kossel and Stranski postulates a lower energy of kink-atom sites compared to step-adatom sites, which is due to the higher number of direct neighbors.[87,88] Both could lower the activation energy for the uptake of Ra^{2+} into an existing step. These assumptions are plausible when comparing the higher energies and hydration of the Ba^{2+} kink-

https://doi.org/10.1021/acs.cgd.4c00416
Cryst. Growth Des. 2024, 24, 7774−7788

sites with the sites for step growth from the simulations with CMD from this study. Both factors compensate for the higher energies due to the necessary lattice distortion. The uptake of Ra^{2+} into the barite structure is thermodynamically less favored than the uptake of Ba^{2+} because the lattice distortions increase the enthalpy of formation.[9] A preferential uptake of Ra^{2+} compared to Ba^{2+} is caused by easier dehydration and is thus a purely kinetically controlled process.

The rate-limiting step for barite growth is kink-site nucleation as a necessary first step to condition step growth.[19,30,31] Ra^{2+} exhibits higher activation energies at all of the sites. Small uncertainties in the hydration enthalpies in the literature (e.g.,[61,66]) used in our analysis is unlikely to affect the conclusions. Because the activation energies determined in this study for nucleation at the kink sites of Ba^{2+} and Ra^{2+} differ by at least 4 kJ/mol at each site, a preferential uptake of Ra^{2+} at these sites can be excluded. It can therefore be assumed that the rate-limiting step for the obtuse and acute steps is Ba^{2+} kink-site nucleation even in the presence of Ra^{2+}. The influence of Ra^{2+} on the kinetics of barite crystal growth can therefore be considered as small.

Estimation of the Entropy Contributions to the Gibbs Free Energy of Ba^{2+} Attachment and Ra^{2+} Uptake Processes during Barite (001) Crystal Growth and (Ba,Ra)SO_4 Solid Solution Formation. The entropies of Ba^{2+} hydration according to Shock et al.[94] are 0.096 and 0.054 kJ/mol K for Ra^{2+}. We note that these are not the absolute values but scaled to the poorly constrained entropy of a hydrated proton. Nevertheless, the entropy contributions could influence the free energy by up to ∼ 12 kJ/mol between the start- and end-structure for the Ra^{2+} attachment and the equivalent structure for Ba^{2+} attachment at 298 K. The entropy effects on the activation energies derived here were estimated by comparing the entropy simulated with the 2PT approach[84−86] for the fully dissolved Ba^{2+} ion and for the Ba^{2+} ion at the acute-low step-adatom position. These configurations were selected for the test because the highest degree of dehydration and thus largest change in entropy are consequently expected during Ba^{2+} kink-site nucleation to this site.

To validate our 2PT approach, we calculated the entropy of H_2O(l) in the simulation cells shown in Figure 2a. Considering the entropy of all 397 water molecules, we obtained the average value for H_2O of 69.2 and 70.1 J/mol K for the start- and end-structures, respectively. Both values correspond well to the literature value for an entropy of H_2O(l) of 69.9 J/mol K.[95]

The obtained entropy of the fully dissolved Ba^{2+} ion is 2.78 J/mol K lower than the entropy of the fully attached Ba^{2+} ions at the acute-low kink-site. This value lowers the free energies of the start-structure compared to the end-structure by ∼ 0.83 kJ/mol at 298 K. Such a small influence of entropy on the computed here activation energies can therefore be neglected.

The slightly higher energies of the Ra^{2+} end structures would also cause an increase in the activation barriers for the Ra^{2+} attachment compared to the Ba^{2+} attachment at the equivalent sites.[29] Even in the extreme case with an energy difference of 12 kJ/mol, the statement would remain unaffected. With such a difference, the kink-site nucleation performed by Ba^{2+} attachment is also preferential compared to that performed by Ra^{2+} attachment. The trend that Ra^{2+} attachment vs Ba^{2+} attachment at sites, which require a higher dehydration is thus not influenced by the entropy contribution.

CONCLUSIONS

New insights into the processes of barite (001) growth and Ra^{2+} uptake in barite at the molecular scale were taken by comparing the Ba^{2+} and Ra^{2+} attachment processes via a CMD and a DFT continuum solvation approach. For the first time, all Ba^{2+} and Ra^{2+} kink-site nucleation processes at the ⟨120⟩ steps of the (001) surface relevant for barite crystal growth were fully assessed, with respect to the attachment paths and activation energies.

Ba^{2+} kink-sites at acute-low and obtuse-low are more strongly embedded and dehydrated into the barite structure than acute-high and obtuse-high due to more chemical bonds to the barite surface and the respective site geometries. Due to the step geometries, kink-sites at the acute steps have a higher degree of dehydration to the respective kink-sites at the obtuse steps. A larger embedded kink-site into the barite structure have a more "bulk-like" configuration and lower energies.

During the formation of a kink site, the complete Ba^{2+} attachment processes are similar for the different possible sites but only up to the formation of the respective inner sphere complexes. Therefore, the barite step morphology only plays a minor role for this process. Differences between the Ba^{2+}-ion attachment pathways at different sites were mainly observed between escape from the inner sphere complex and complete attachment. The formation of more strongly embedded kink-sites of a low position requires more dehydration steps and steps to form chemical bonds. This leads to longer and more complicated attachment pathways with higher activation energies. However, this is also the case of kink-site detachment. A higher stability of the kink-sites at the acute-low and obtuse-low positions and, therefore, a greater relevance for barite growth can be assumed. The formation of the Ba^{2+} kink-site at the obtuse-low site is favored by the lower required degree of dehydration due to the more open step geometry. The obtuse step is therefore likely to be the fast-growing step at the barite (001)-water interface.

The simulations of the last steps of Ba^{2+} attachment for barite ⟨120⟩ step growth at all sites indicate different growth rates of the obtuse and acute steps. A difficult rate-limiting kink-site nucleation and rather uniform attachment of Ba^{2+} during step growth in both ⟨120⟩ directions indicate slow straight acute step growth. Easier kink-site nucleation at the obtuse step and preferential Ba^{2+} addition during step growth in one direction indicate rapid growth of a curved step. An interplay of growth of both steps could explain the observed curved obtuse step in microscopic studies by molecular scale processes. Kinetic Monte Carlo simulations using the results of this study could further close the gap between the atomic scale and microscopically observed barite growth.

The process of Ra^{2+} kink-site nucleation is similar to that of Ba^{2+} kink-site nucleation as similar bonds are formed in the same order. However, the lattice distortions increase the activation energies of the Ra^{2+} kink-site nucleation. The lattice distortion is more pronounced in Ra^{2+} step-adatoms, which are located on the barite surface. The rate-limiting steps for barite crystal growth on the (001) surface at both steps are thus determined mainly by the kink-site nucleation of Ba^{2+} [Figure 8(1)], and only minor effects of Ra^{2+} on the kinetics of barite growth can be assumed. However, kink-site nucleation processes at sites that require a higher lattice distortion also require a higher degree of dehydration, which is easier for Ra^{2+} than for Ba^{2+}. The activation energies of kink-site nucleation

https://doi.org/10.1021/acs.cgd.4c00416
Cryst. Growth Des. 2024, 24, 7774−7788

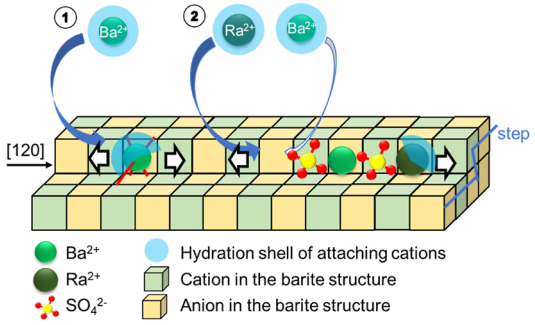

Figure 8. Illustration of the barite crystal growth and Ra uptake into the barite crystal structure at the barite (001)—water interface according to this study. (1) Rate-limiting process of kink-site nucleation, which occurs preferentially by Ba^{2+} attachment compared to Ra^{2+} uptake. (2) Step-growth by preferential uptake of Ra^{2+} compared to Ba^{2+} attachment.

where the step-adatoms are more "bulk-like" are therefore more similar to the corresponding Ba^{2+} kink-site nucleation processes. During Ra^{2+} kink-site nucleation, the higher dehydration increasingly compensates for the higher activation energies of the necessary lattice distortion.

Thus, with further step growth, Ra^{2+} could be preferentially taken up during the not rate-limiting ⟨120⟩ step growth despite higher energy due to the necessary lattice distortion, which is in good agreement with the preferred kinetically controlled Ra^{2+} uptake observed by Weber et al.[18] [Figure 8(2)].

■ ASSOCIATED CONTENT

Supporting Information

The Supporting Information is available free of charge at https://pubs.acs.org/doi/10.1021/acs.cgd.4c00416.

Comparison of the guessed states of the Ba^{2+} and Ra^{2+} kink-site nucleation processes. All structures calculated in this study are available in the data publication: 10.26165/JUELICH-DATA/TMXM7D (PDF)

■ AUTHOR INFORMATION

Corresponding Author

Stefan Rudin − *Institute of Fusion Energy and Nuclear Waste Management (IFN-2)—Nuclear Waste Management, Forschungszentrum Jülich GmbH, Jülich 52425, Germany;* orcid.org/0000-0002-4857-7322; Phone: +49 2461 61 6702; Email: s.rudin@fz-juelich.de

Authors

Piotr M. Kowalski − *Institute of Energy Technologies (IET-3)—Theory and Computation of Energy Materials, Forschungszentrum Jülich GmbH, Jülich 52425, Germany; Jülich Aachen Research Alliance JARA Energy & Center for Simulation and Data Science (CSD), Jülich 52425, Germany;* orcid.org/0000-0001-6604-3458

Martina Klinkenberg − *Institute of Fusion Energy and Nuclear Waste Management (IFN-2)—Nuclear Waste Management, Forschungszentrum Jülich GmbH, Jülich 52425, Germany*

Dirk Bosbach − *Institute of Fusion Energy and Nuclear Waste Management (IFN-2)—Nuclear Waste Management, Forschungszentrum Jülich GmbH, Jülich 52425, Germany*

Felix Brandt − *Institute of Fusion Energy and Nuclear Waste Management (IFN-2)—Nuclear Waste Management, Forschungszentrum Jülich GmbH, Jülich 52425, Germany*

Complete contact information is available at: https://pubs.acs.org/10.1021/acs.cgd.4c00416

Notes

The authors declare no competing financial interest.

■ ACKNOWLEDGMENTS

We thank Andrew Stack for useful discussions and explanation of previous classical molecular simulations of $BaSO_4$ workflow, including the applied force field. We acknowledge substantial help we obtained from Fabian Tipp in performing 2PT simulations. The research leading to these results has received funding from the German Federal Ministry of Education and Research (BMBF) KRIMI project (project number 02NUK056B). The authors gratefully acknowledge the computing time granted by the JARA Vergabegremium and provided on the JARA Partition part of the supercomputers JURECA at Forschungszentrum Jülich and CLAIX at RWTH Aachen University (Project cjiek61).

■ REFERENCES

(1) Ceccarello, S.; Black, S.; Read, D.; Hodson, M. E. Industrial radioactive Barite scale: suppression of radium uptake by introduction of competing ions. *Miner. Eng.* **2004**, *17* (2), 323−330.

(2) Martin, A. J.; Crusius, J.; McNee, J. J.; Yanful, E. K. The mobility of radium-226 and trace metals in pre-oxidized subaqueous uranium mill tailings. *Appl. Geochem.* **2003**, *18* (7), 1095−1110.

(3) Rutherford, P.; Dudas, M.; Arocena, J. Heterogeneous distribution of radionuclides, barium and strontium in phosphogypsum by-product. *Sci. Total Environ.* **1996**, *180* (3), 201−209.

(4) Fisher, R. S. Geologic and geochemical controls on naturally occurring radioactive materials (NORM) in produced water from oil, gas, and geothermal operations. *Environ. Geosci.* **1998**, *5* (3), 139−150.

(5) SKB. Long-term safety for the final repository for spent nuclear fuel at Forsmark. *Main Report of the SR-Site Project*; Swedish Nuclear Fuel and Waste Management Co Stockholm, 2011; Vol. *1*, p 892.

(6) Brandt, F.; Curti, E.; Klinkenberg, M.; Rozov, K.; Bosbach, D. Replacement of Barite by a (Ba, Ra) SO4 solid solution at close-to-equilibrium conditions: A combined experimental and theoretical study. *Geochem. Cosmochim. Acta* **2015**, *155*, 1−15.

(7) Curti, E.; Fujiwara, K.; Iijima, K.; Tits, J.; Cuesta, C.; Kitamura, A.; Glaus, M. a.; Müller, W. Radium uptake during barite recrystallization at 23±2°C as a function of solution composition: An experimental 133Ba and 226Ra tracer study. *Geochim. Cosmochim. Acta* **2010**, *74* (12), 3553−3570.

(8) Klinkenberg, M.; Brandt, F.; Breuer, U.; Bosbach, D. Uptake of Ra during the recrystallization of Barite: a microscopic and time of flight-secondary ion mass spectrometry study. *Environ. Sci. Technol.* **2014**, *48* (12), 6620−6627.

(9) Vinograd, V.; Brandt, F.; Rozov, K.; Klinkenberg, M.; Refson, K.; Winkler, B.; Bosbach, D. Solid-aqueous equilibrium in the BaSO4-RaSO4-H2O system: first-principles calculations and a thermodynamic assessment. *Geochim. Cosmochim. Acta* **2013**, *122*, 398−417.

(10) Heberling, F.; Metz, V.; Böttle, M.; Curti, E.; Geckeis, H. Barite recrystallization in the presence of 226Ra and 133Ba. *Geochim. Cosmochim. Acta* **2018**, *232*, 124−139.

(11) Doerner, H. A.; Hoskins, W. M. Co-precipitation of radium and barium sulfates. *J. Am. Chem. Soc.* **1925**, *47*, 662−675.

(12) Poonoosamy, J.; Kaspor, A.; Schreinemachers, C.; Bosbach, D.; Cheong, O.; Kowalski, P. M.; Obaied, A. A radiochemical lab-on-a-chip paired with computer vision to unlock the crystallization kinetics of (Ba, Ra) SO4. *Sci. Rep.* **2024**, *14* (1), 9502.

(13) Rosenberg, Y. O.; Metz, V.; Ganor, J. Co-precipitation of radium in high ionic strength systems: 1. Thermodynamic properties of the Na-Ra-Cl-SO(4)-H(2)O system—Estimating Pitzer parameters for RaCl(2). *Geochim. Cosmochim. Acta* **2011**, *75* (19), 5389−5402.
(14) Rosenberg, Y. O.; Metz, V.; Ganor, J. Radium removal in a large scale evaporitic system. *Geochim. Cosmochim. Acta* **2013**, *103*, 121−137.
(15) Rosenberg, Y. O.; Metz, V.; Oren, Y.; Volkman, Y.; Ganor, J. Co-precipitation of radium in high ionic strength systems: 2. Kinetic and ionic strength effects. *Geochim. Cosmochim. Acta* **2011**, *75* (19), 5403−5422.
(16) Rosenberg, Y. O.; Sade, Z.; Ganor, J. The precipitation of gypsum, celestine, and Barite and coprecipitation of radium during seawater evaporation. *Geochim. Cosmochim. Acta* **2018**, *233*, 50−65.
(17) Rosenberg, Y. O.; Sadeh, Y.; Metz, V.; Pina, C. M.; Ganor, J. Nucleation and growth kinetics of RaxBa1- xSO4 solid solution in NaCl aqueous solutions. *Geochim. Cosmochim. Acta* **2014**, *125*, 290−307.
(18) Weber, J.; Barthel, J.; Klinkenberg, M.; Bosbach, D.; Kruth, M.; Brandt, F. Retention of 226Ra by Barite: The role of internal porosity. *Chem. Geol.* **2017**, *466*, 722−732.
(19) Bosbach, D. Linking molecular-scale Barite precipitation mechanisms with macroscopic crystal growth rates. In *Water-Rock Interactions, Ore Deposits, and Environmental Geochemistry: A Tribute to David A. Crerar*, Special Pu ed.; Wood, S. A., Hellmann, R., Eds.; The Geochemical Society, 2002; pp 97−110.
(20) Higgins, S. R.; Bosbach, D.; Eggleston, C. M.; Knauss, K. G. Kink dynamics and step growth on barium sulfate (001): a hydrothermal scanning probe microscopy study. *J. Phys. Chem. B* **2000**, *104* (30), 6978−6982.
(21) Pina, C.; Bosbach, D.; Prieto, M.; Putnis, A. Microtopography of the barite (0 0 1) face during growth: *J. Cryst. Growth* **1998**, *187* (1), 119−125.
(22) Pina, C. M.; Becker, U.; Risthaus, P.; Bosbach, D.; Putnis, A. Molecular-scale mechanisms of crystal growth in Barite. *Nature* **1998**, *395* (6701), 483−486.
(23) Poonoosamy, J.; Haber-Pohlmeier, S.; Deng, H.; Deissmann, G.; Klinkenberg, M.; Gizatullin, B.; Stapf, S.; Brandt, F.; Bosbach, D.; Pohlmeier, A. Combination of MRI and SEM to assess changes in the chemical properties and permeability of porous media due to Barite precipitation. *Minerals* **2020**, *10* (3), 226.
(24) Poonoosamy, J.; Obaied, A.; Deissmann, G.; Prasianakis, N. I.; Kindelmann, M.; Wollenhaupt, B.; Bosbach, D.; Curti, E. Microfluidic investigation of pore-size dependency of Barite nucleation. *Commun. Chem.* **2023**, *6* (1), 250.
(25) Weber, J.; Barthel, J.; Brandt, F.; Klinkenberg, M.; Breuer, U.; Kruth, M.; Bosbach, D. Nano-structural features of Barite crystals observed by electron microscopy and atom probe tomography. *J. Cryst. Growth* **2016**, *424*, 51−59.
(26) Allan, N. L.; Rohl, A. L.; Gay, D. H.; Catlow, C. R. A.; Davey, R. J.; Mackrodt, W. C. Calculated bulk and surface properties of sulfates. *Faraday Discuss.* **1993**, *95* (0), 273−280.
(27) Bittarello, E.; Bruno, M.; Aquilano, D. Ab initio calculations of the main crystal surfaces of baryte (BaSO4). *Cryst. Growth Des.* **2018**, *18* (7), 4084−4094.
(28) Godinho, J. R.; Stack, A. G. Growth kinetics and morphology of Barite crystals derived from face-specific growth rates. *Cryst. Growth Des.* **2015**, *15* (5), 2064−2071.
(29) Rudin, S.; Kowalski, P. M.; Klinkenberg, M.; Bornhake, T.; Bosbach, D.; Brandt, F. Simulation of Crystal Growth by an Innovative Hybrid Density Functional Theory Continuum Solvation Approach: Kink Site Formation on Barite (001). *Cryst. Growth Des.* **2024**, *24* (1), 159−170.
(30) Bracco, J. N.; Gooijer, Y.; Higgins, S. R. Hydrothermal atomic force microscopy observations of Barite step growth rates as a function of the aqueous barium-to-sulfate ratio. *Geochim. Cosmochim. Acta* **2016**, *183*, 1−13.
(31) Pina, C. M.; Jordan, G., Reactivity of mineral surfaces at nanoscale: kinetics and mechanisms of growth and dissolution. **2010**.239, 323, ,
(32) de Antonio Gomez, S.; Pina, C. M.; Martin-Bragado, I. Lattice kinetic modeling of the anisotropic growth of two-dimensional islands on Barite (001) surface. *Cryst. Growth Des.* **2013**, *13* (7), 2840−2845.
(33) Stack, A. G. Molecular dynamics simulations of solvation and Kink Site formation at the {001} Barite- Water interface. *J. Phys. Chem. C* **2009**, *113* (6), 2104−2110.
(34) Stack, A. G.; Raiteri, P.; Gale, J. D. Accurate rates of the complex mechanisms for growth and dissolution of minerals using a combination of rare-event theories. *J. Am. Chem. Soc.* **2012**, *134* (1), 11−14.
(35) Kowacz, M.; Putnis, C.; Putnis, A. The effect of cation: anion ratio in solution on the mechanism of Barite growth at constant supersaturation: Role of the desolvation process on the growth kinetics. *Geochem. Cosmochim. Acta* **2007**, *71* (21), 5168−5179.
(36) Momma, K.; Izumi, F. VESTA 3 for three-dimensional visualization of crystal, volumetric and morphology data. *J. Appl. Crystallogr.* **2011**, *44* (6), 1272−1276.
(37) Kurganskaya, I.; Rohlfs, R. D. Atomistic to meso-scale modeling of mineral dissolution: Methods, challenges and prospects. *Am. J. Sci.* **2020**, *320* (1), 1−26.
(38) Kurganskaya, I.; Trofimov, N.; Luttge, A. A kinetic Monte Carlo approach to model Barite dissolution: the role of reactive site geometry. *Minerals* **2022**, *12* (5), 639.
(39) Jang, Y. H.; Chang, X. Y.; Blanco, M.; Hwang, S.; Tang, Y.; Shuler, P.; Goddard, W. A. The MSXX force field for the barium sulfate- water interface. *J. Phys. Chem. B* **2002**, *106* (38), 9951−9966.
(40) Stack, A. G.; Rustad, J. R. Structure and dynamics of water on aqueous barium ion and the {001} Barite surface. *J. Phys. Chem. C* **2007**, *111* (44), 16387−16391.
(41) Martínez, L.; Andrade, R.; Birgin, E. G.; Martínez, J. M. PACKMOL: A package for building initial configurations for molecular dynamics simulations. *J. Comput. Chem.* **2009**, *30* (13), 2157−2164.
(42) Rudin, S.; Kowalski, P.; Klinkenberg, M.; Bosbach, D.; Brandt, F. *Simulation Data for: The Anisotropy of Barite during Crystal Growth and the Uptake of Radium*, V1 ed.; Jülich DATA, 2024.
(43) Gale, J. D. GULP: A computer program for the symmetry-adapted simulation of solids. *J. Chem. Soc., Faraday Trans.* **1997**, *93* (4), 629−637.
(44) Gale, J. D.; Rohl, A. L. The general utility lattice program (GULP). *Mol. Simul.* **2003**, *29* (5), 291−341.
(45) Levitt, M.; Hirshberg, M.; Sharon, R.; Laidig, K. E.; Daggett, V. Calibration and testing of a water model for simulation of the molecular dynamics of proteins and nucleic acids in solution. *J. Phys. Chem. B* **1997**, *101* (25), 5051−5061.
(46) Eisenberg, D.; Kauzmann, W. *The Structure and Properties of Water*; OUP Oxford, 2005.
(47) Hoover, W. G. Canonical dynamics: Equilibrium phase-space distributions. *Phys. Rev. A* **1985**, *31* (3), 1695−1697.
(48) Nosé, S. A unified formulation of the constant temperature molecular dynamics methods. *J. Chem. Phys.* **1984**, *81* (1), 511−519.
(49) Nosé, S. An extension of the canonical ensemble molecular dynamics method. *Mol. Phys.* **1986**, *57* (1), 187−191.
(50) Fisicaro, G.; Genovese, L.; Andreussi, O.; Mandal, S.; Nair, N. N.; Marzari, N.; Goedecker, S. Soft-sphere continuum solvation in electronic-structure calculations. *J. Chem. Theor. Comput.* **2017**, *13* (8), 3829−3845.
(51) Giannozzi, P.; Andreussi, O.; Brumme, T.; Bunau, O.; Buongiorno Nardelli, M.; Calandra, M.; Car, R.; Cavazzoni, C.; Ceresoli, D.; Cococcioni, M.; et al. Advanced capabilities for materials modelling with Quantum ESPRESSO. *J. Phys. Condens. Matter* **2017**, *29* (46), 465901.
(52) Giannozzi, P.; Baroni, S.; Bonini, N.; Calandra, M.; Car, R.; Cavazzoni, C.; Ceresoli, D.; Chiarotti, G. L.; Cococcioni, M.; Dabo, I.; Dal Corso, A.; de Gironcoli, S.; Fabris, S.; Fratesi, G.; Gebauer, R.; Gerstmann, U.; Gougoussis, C.; Kokalj, A.; Lazzeri, M.; Martin-

https://doi.org/10.1021/acs.cgd.4c00416
Cryst. Growth Des. 2024, 24, 7774−7788

Samos, L.; Marzari, N.; Mauri, F.; Mazzarello, R.; Paolini, S.; Pasquarello, A.; Paulatto, L.; Sbraccia, C.; Scandolo, S.; Sclauzero, G.; Seitsonen, A. P.; Smogunov, A.; Umari, P.; Wentzcovitch, R. M. QUANTUM ESPRESSO: a modular and open-source software project for quantum simulations of materials. *J. Phys.: Condens. Matter* **2009**, *21* (39), 395502.
(53) Perdew, J. P.; Burke, K.; Ernzerhof, M. Generalized gradient approximation made simple. *Phys. Rev. Lett.* **1996**, *77* (18), 3865−3868.
(54) Vanderbilt, D. Soft self-consistent pseudopotentials in a generalized eigenvalue formalism. *Phys. Rev. B* **1990**, *41* (11), 7892−7895.
(55) Matyskin, A. V.; Ylmen, R.; Lagerkvist, P.; Ramebäck, H.; Ekberg, C. Crystal structure of radium sulfate: an X-ray powder diffraction and density functional theory study. *J. Solid State Chem.* **2017**, *253*, 15−20.
(56) Perdew, J. P.; Ruzsinszky, A.; Csonka, G. I.; Vydrov, O. A.; Scuseria, G. E.; Constantin, L. A.; Zhou, X.; Burke, K. Restoring the density-gradient expansion for exchange in solids and surfaces. *Phys. Rev. Lett.* **2008**, *100* (13), 136406.
(57) Andreussi, O.; Dabo, I.; Marzari, N. Revised self-consistent continuum solvation in electronic-structure calculations. *J. Chem. Phys.* **2012**, *136* (6), 064102.
(58) Andreussi, O.; Hormann, N. G.; Nattino, F.; Fisicaro, G.; Goedecker, S.; Marzari, N. Solvent-aware interfaces in continuum solvation. *J. Chem. Theor. Comput.* **2019**, *15* (3), 1996−2009.
(59) Rappe, A. K.; Casewit, C. J.; Colwell, K.; Goddard, W. A., III; Skiff, W. M. UFF, a full periodic table force field for molecular mechanics and molecular dynamics simulations. *J. Am. Chem. Soc.* **1992**, *114* (25), 10024−10035.
(60) Shannon, R. D. Revised effective ionic radii and systematic studies of interatomic distances in halides and chalcogenides. *Acta Crystallogr. Sect. A Cryst. Phys. Diffr. Theor. Gen. Crystallogr.* **1976**, *32* (5), 751−767.
(61) Smith, D. W. Ionic hydration enthalpies. *J. Chem. Educ.* **1977**, *54* (9), 540.
(62) Bracco, J. N.; Lee, S. S.; Stubbs, J. E.; Eng, P. J.; Heberling, F.; Fenter, P.; Stack, A. G. Hydration structure of the Barite (001)-water interface: Comparison of x-ray reflectivity with molecular dynamics simulations. *J. Phys. Chem. C* **2017**, *121* (22), 12236−12248.
(63) Fenter, P.; McBride, M.; Srajer, G.; Sturchio, N.; Bosbach, D. Structure of Barite (001)- and (210)- water interfaces. *J. Phys. Chem. B* **2001**, *105* (34), 8112−8119.
(64) Chibowski, E.; Hołysz, L. Influence of tetradecylamine chloride on the surface free-energy components and flotability of Barite. *J. Mater. Sci.* **1992**, *27*, 5221−5228.
(65) Vital, M.; Daval, D.; Morvan, G.; Martinez, D. E.; Heap, M. J. Barite growth rates as a function of crystallographic orientation, temperature, and solution saturation state. *Cryst. Growth Des.* **2020**, *20* (6), 3663−3672.
(66) Marcus, Y. Thermodynamics of solvation of ions. Part 5.—Gibbs free energy of hydration at 298.15 K. *J. Chem. Soc., Faraday Trans.* **1991**, *87* (18), 2995−2999.
(67) Housecroft, C. E.; Brooke Jenkins, H. D. Absolute ion hydration enthalpies and the role of volume within hydration thermodynamics. *RSC Adv.* **2017**, *7* (45), 27881−27894.
(68) Chaudhari, M. I.; Soniat, M.; Rempe, S. B. Octa-coordination and the aqueous Ba2+ ion. *J. Phys. Chem. B* **2015**, *119* (28), 8746−8753.
(69) D'Angelo, P.; Pavel, N.; Roccatano, D.; Nolting, H.-F. Multielectron excitations at the L edges of barium in aqueous solution. *Phys. Rev. B* **1996**, *54* (17), 12129−12138.
(70) Hofer, T. S.; Rode, B. M.; Randolf, B. R. Structure and dynamics of solvated Ba (II) in dilute aqueous solution-an ab initio QM/MM MD approach. *Chem. Phys.* **2005**, *312* (1−3), 81−88.
(71) Larentzos, J. P.; Criscenti, L. J. A molecular dynamics study of alkaline earth metal- chloride complexation in aqueous solution. *J. Phys. Chem. B* **2008**, *112* (45), 14243−14250.
(72) Mamatkulov, S.; Schwierz, N. Force fields for monovalent and divalent metal cations in TIP3P water based on thermodynamic and kinetic properties. *J. Chem. Phys.* **2018**, *148* (7), 074504.
(73) Migliorati, V.; Caruso, A.; D'Angelo, P. Unraveling the hydration properties of the Ba2+ aqua ion: the interplay of quantum mechanics, molecular dynamics, and EXAFS spectroscopy. *Inorg. Chem.* **2019**, *58* (21), 14551−14559.
(74) Pappalardo, R. R.; Caralampio, D. Z.; Martínez, J. M.; Sanchez Marcos, E. Hydration of Heavy Alkaline-Earth Cations Studied by Molecular Dynamics Simulations and X-ray Absorption Spectroscopy. *Inorg. Chem.* **2021**, *60* (17), 13578−13587.
(75) Persson, I.; Sandström, M.; Yokoyama, H. Structure of the solvated strontium and barium ions in aqueous, dimethyl sulfoxide and pyridine solution, and crystal structure of strontium and barium hydroxide octahydrate. *Zeitschrift für Naturforschung A* **1995**, *50* (1), 21−37.
(76) Raiteri, P.; Demichelis, R.; Gale, J. D. Thermodynamically consistent force field for molecular dynamics simulations of alkaline-earth carbonates and their aqueous speciation. *J. Phys. Chem. C* **2015**, *119* (43), 24447−24458.
(77) Matsuda, A.; Mori, H. Theoretical Study on the Hydration Structure of Divalent Radium Ion Using Fragment Molecular Orbital-Molecular Dynamics (FMO-MD) Simulation. *J. Solution Chem.* **2014**, *43* (9−10), 1669−1675.
(78) Henkelman, G.; Jónsson, H. A dimer method for finding saddle points on high dimensional potential surfaces using only first derivatives. *J. Chem. Phys.* **1999**, *111* (15), 7010−7022.
(79) Henkelman, G.; Jónsson, H. Improved tangent estimate in the nudged elastic band method for finding minimum energy paths and saddle points. *J. Chem. Phys.* **2000**, *113* (22), 9978−9985.
(80) Henkelman, G.; Uberuaga, B. P.; Jónsson, H. A climbing image nudged elastic band method for finding saddle points and minimum energy paths. *J. Chem. Phys.* **2000**, *113* (22), 9901−9904.
(81) Jónsson, H.; Mills, G.; Jacobsen, K. W. Nudged elastic band method for finding minimum energy paths of transitions. In *Classical and Quantum Dynamics in Condensed Phase Simulations*; World Scientific, 1998; pp 385−404.
(82) Sheppard, D.; Henkelman, G. Paths to which the nudged elastic band converges. *J. Comput. Chem.* **2011**, *32* (8), 1769−1771.
(83) Cheong, O.; Tipp, F. P.; Eikerling, M. H.; Kowalski, P. M. Entropy Effects on Reactive Processes at Metal-Solvent Interfaces. *J. Phys. Chem. C* **2024**, *128*, 7892−7902.
(84) Lin, S.-T.; Blanco, M.; Goddard, W. A., III The two-phase model for calculating thermodynamic properties of liquids from molecular dynamics: Validation for the phase diagram of Lennard-Jones fluids. *J. Chem. Phys.* **2003**, *119* (22), 11792−11805.
(85) Lin, S.-T.; Maiti, P. K.; Goddard, W. A., III Two-phase thermodynamic model for efficient and accurate absolute entropy of water from molecular dynamics simulations. *J. Phys. Chem. B* **2010**, *114* (24), 8191−8198.
(86) Pascal, T. A.; Lin, S.-T.; Goddard, W. A., III Thermodynamics of liquids: standard molar entropies and heat capacities of common solvents from 2PT molecular dynamics. *Phys. Chem. Chem. Phys.* **2011**, *13* (1), 169−181.
(87) Kossel, W. Extending the law of Bravais. *Nachr. Ges. Wiss. Göttingen* **1927**, *143*, 135−143.
(88) Stranski, I. N. Zur theorie des kristallwachstums. *Zeitschrift für physikalische Chemie* **1928**, *136U* (1), 259−278.
(89) Hillner, P.; Manne, S.; Gratz, A.; Hansma, P. AFM images of dissolution and growth on a calcite crystal. *Ultramicroscopy* **1992**, *42−44*, 1387−1393.
(90) Teng, H. H.; Dove, P. M.; De Yoreo, J. J. Kinetics of calcite growth: surface processes and relationships to macroscopic rate laws. *Geochim. Cosmochim. Acta* **2000**, *64* (13), 2255−2266.
(91) Teng, H. H.; Dove, P. M.; Orme, C. A.; De Yoreo, J. J. Thermodynamics of calcite growth: baseline for understanding biomineral formation. *Science* **1998**, *282* (5389), 724−727.
(92) Higgins, S. R.; Jordan, G.; Eggleston, C. M.; Knauss, K. G. Dissolution kinetics of the barium sulfate (001) surface by

https://doi.org/10.1021/acs.cgd.4c00416
Cryst. Growth Des. 2024, 24, 7774−7788

hydrothermal atomic force microscopy. *Langmuir* **1998**, *14* (18), 4967−4971.
(93) Kurganskaya, I.; Luttge, A. Mineral Dissolution Kinetics: Pathways to Equilibrium. *ACS Earth Space Chem.* **2021**, *5* (7), 1657−1673.
(94) Shock, E. L.; Sassani, D. C.; Willis, M.; Sverjensky, D. A. Inorganic species in geologic fluids: correlations among standard molal thermodynamic properties of aqueous ions and hydroxide complexes. *Geochim. Cosmochim. Acta* **1997**, *61* (5), 907−950.
(95) Dean, J. A. *Lange's Handbook of Chemistry*; Mcgraw-Hill, Inc., 1999.

https://doi.org/10.1021/acs.cgd.4c00416
Cryst. Growth Des. 2024, 24, 7774−7788